Spatial and Temporal Variability of North Atlantic Eddy Field at Scale less than 100km.

A. O. Ajayi[1], **J. Le Sommer**[1], **E. Chassignet**[2], **JM. Molines**[1], **X. Xu**[2], **A. Albert**[1], and **E. Cosme**[1]

[1]Universite Grenoble Alpes /CNRS/IGE, Grenoble, France.
[2]Florida State University, Tallahassee, USA.

This is a non-peer reviewed preprint submitted to ESSOAr.
This manuscript has been submitted on the 30th of October 2019, to the Journal of Geophysical Research-Oceans.

Abstract

Ocean circulation is dominated by turbulent geostrophic eddy fields with typical scales ranging from 10 km to 300 km. At mesoscales (¿ 50 km), the size of eddy structures varies regionally following the Rossby radius of deformation. The variability of the scale of smaller eddies is not well known due to the limitations in existing numerical simulations and satellite capability. But it is well established that oceanic flows (¡ 50km) generally exhibit strong seasonality. In this study, we present a basin-scale analysis of coherent structures down to 10 km in the North Atlantic Ocean using two submesoscale-permitting ocean models, a NEMO-based North Atlantic simulation with a horizontal resolution of 1/60 (NATL60) and an HYCOM-based Atlantic simulation with a horizontal resolution of 1/50 (HYCOM50). We investigate the spatial and temporal variability of the scale of eddy structures with a particular focus on eddies with scales of 10 to 100 km, and examine the impact of the seasonality of submesoscale energy on the seasonality and distribution of coherent structures in the North Atlantic. Our results show an overall good agreement between the two models in terms of surface wavenumber spectra and seasonal variability. The key findings of the paper are that (i) the mean size of ocean eddies show strong seasonality; (ii) this seasonality is associated with an increased population of submesoscale eddies (10 – 50 km) in winter; and (iii) the net release of available potential energy associated with mixed layer instability is responsible for the emergence of the increased population of submesoscale eddies in wintertime.

1 Introduction

Ocean circulation combines large ($>500\,\mathrm{km}$), meso ($50-500\,\mathrm{km}$) and submesoscale ($1-50\,\mathrm{km}$) structures that result from direct forcing and energy exchanges through nonlinear scale interactions. The ocean is a turbulent fluid and most of its energy is concentrated in geostrophically balanced eddy fields. The coherent structures that make up the eddy field are mostly generated by baroclinic instability in an intensified ocean flow (Stammer, 1997) and therefore scale with the first Rossby radius of deformation. These ubiquitous, energetic, time-dependent circulations have their signature in all aspects of ocean activities and have, therefore, been defined as the weather system of the ocean (Bryan, 2008; McWilliams, 2016).

Improving our knowledge of the scale of eddy structures is key to several applications in physical oceanography. The interaction between the eddy field and large-scale flow is one of the main drivers of ocean circulation. This interaction is presently parameterized in non-eddy resolving ocean and climate models and the parameterizations used in these models are usually derived from a mixing length hypothesis based on eddy velocity and eddy length scale to derive eddy diffusivity (Fox-Kemper et al., 2008; Bates et al., 2014). The correlation scale of mesoscale eddies is also central to the design of the inversion algorithm used in satellite remote sensing. For instance, the optimal interpolation method currently used in calibrating AVISO products takes as input correlation radii based on eddy length scales (Ducet and Traon, 2001). If the typical scale of eddies varies in time and space in the ocean, then this variability should be accounted for in ocean model parameterizations schemes and in satellite data interpolation algorithms, hence the need to document how eddy scale vary in space and time.

Satellite missions have revolutionized the way we see the Earth surface from space and continue to serve as a large-scale observational platform for modern oceanography. Satellite data are currently the major source of knowledge about oceanic eddies,their scales and their variability. A concise review of the knowledge gained from using satellite altimeters to study mesoscale eddies in the global ocean is presented in Fu et al. (2010). Early works include a regional study on the variability of mesoscale eddies using Geosat by Le Traon et al. (1990), where the authors inferred scales of eddies from the spatial autocorrelation function of observed sea surface height (SSH) fields and recorded a high variability of mesoscale eddy fields in space across the entire North Atlantic. More recently, the merging of altimeter products covering a 16-year period paved the way for the automated identification, tracking, and documentation of about 35,000 mesoscale eddies with a lifetime greater than 16 weeks (Chelton et al., 2011). This analysis confirmed that the observed eddy scales mostly fall between the first Rossby radius of deformation L_d and the Rhines scale L_d (Klocker and Abernathey, 2014). This is in agreement with Eden (2007) who

found in an eddy-permitting numerical simulation of the North Atlantic that north of 30°N eddy scales are isotropic and proportional to L_d, while south of 30°N the eddies' scales are more closely related to the L_r. The scale $\min(L_r,L_d)$ was found to be the best predictor of eddy scale over the entire North Atlantic domain.

Studies focusing on coherent eddy structures in the ocean have mostly been limited to structures with scales on the order of 100 km (Amores et al., 2018). This is largely due to the non-availability of a high-resolution global oceanic dataset for the smaller wavelength range, a consequence of the limitations of existing numerical and satellite altimetry capability (Dufau et al., 2016). That been said, several ocean models, such as the NEMO-based North Atlantic simulation with a horizontal resolution of 1/60° (NATL60) and the HYCOM-based Atlantic simulation with a horizontal resolution of 1/50° (HYCOM50), were designed in preparation for the upcoming Surface Water and Ocean Topography (SWOT) altimeter mission (Fu and Ubelmann, 2014). These simulations now have the ability to capture explicitly ocean circulation at the basin-scale down to 10 km and therefore provide a platform to investigate the variability of eddy structures at scales less than 100 km.

At scale smaller than 100 km, oceanic flows are dominated by surface-intensified energetic submesoscale motions and they include coherent vortices, fronts, and filaments. Furthermore, both observations and model simulations have shown that submesoscale motions undergo a strong seasonality with large amplitudes in winter (Callies et al., 2015a; Qiu et al., 2014; Sasaki et al., 2014; Brannigan et al., 2015; Rocha et al., 2016). The emergence in winter of submesoscale motions has been attributed to frontogenesis, wind-induced frontal instabilities, and mixed layer instability (Thomas, 2008; McWilliams, 2016). Mixed layer instability (which is associated with the weakening of surface stratification in winter conditions) has been put forward as the dominant mechanism driving the emergence of submesoscales in winter in mid-latitudes (Capet et al., 2008; Mensa et al., 2013; Qiu et al., 2014; Sasaki et al., 2014; Callies et al., 2015b).

In this paper, the emphasis is on eddies with scales < 100 km, with a focus on *coherent structures* within the 10–50 km scale range, hereafter referred to as submesoscale eddies (SMEs) (Sasaki et al., 2017). Our key objective is to investigate how resolving submesoscales affects eddy motions and their variability, specifically in terms of spatial scale and depth penetration. This paper intends to answer this question by documenting the statistics of SMEs and their overall impact on the variability of averaged eddy scales in the North Atlantic. This is done by first performing a basin-scale analysis of the spatial and temporal variability of coherent structures down to 10 km in the North Atlantic Ocean using two submesoscale resolving ocean models, NATL60 and HYCOM50. Then, we examine the impact of the seasonality of submesoscale energy on the distribution and depth penetration of eddy structures in the North Atlantic.

This paper is organized as follows: In section 2, we provide a description of the NATL60 and HYCOM50 datasets. In section 3, we present the description of eddy statistics. Sections 4 focuses on the spatial variability of eddy scales while section 5 presents the seasonality of eddy scales with insights on the impact of mixed layer instability on eddy statistics. We summarize and conclude our analysis in section 6.

2 Datasets and Methodology

2.1 North Atlantic Ocean model simulations

In this study, we use numerical outputs from two submesoscale eddy-permitting simulations of the North Atlantic: a NEMO-based North Atlantic simulation with a horizontal resolution of 1/60° (NATL60) and a HYCOM-based Atlantic simulation with a horizontal resolution of 1/50° (HYCOM50).

The NEMO-based NATL60 has a horizontal grid spacing that ranges from 1.6 km at 26°N to 0.9 km at 65°N. The grid has been designed so that the model explicitly simulates the scales of motions that will be observed by the SWOT altimetric mission. In practice, the model's effective resolution is about 10-15 km in wavelength. The initial and open boundary conditions are based on GLORYS2v3 ocean reanalysis with a relaxation zone at the northern boundary for sea-ice concentration and thickness. The model has 300 vertical levels with a resolution of 1 m at the top-most layers. The atmospheric forcing is based on DFS5.2 (Dussin et al. (2018)). The grid and bathymetry follow Ducousso et al. (2017). In order to implicitly adapt lateral viscosity and diffusivity to flow properties, a third-order upwind advection scheme is used for both momentum and tracers in the model simulation. The model is spun-up for a period of six months, and a one-year simulation output from 2012 to 2013 is used in this study. A description of the NATL60 simulation is available from Le Sommer et al. (2019) and the outputs have been used in recent studies by Fresnay et al. (2018) and Amores et al. (2018).

The HYCOM-based HYCOM50 extends from 28°S to 80°N and has a horizontal grid spacing ranging from 2.25 km at the equator, $\sim$1.5 km in the Gulf Stream region, and 1 km in the subpolar gyre. As for NATL60, the effective resolution is about 10–15 km. The vertical coordinate is hybrid and consists of 32 layers. The simulation is initialized using potential temperature and salinity from the GDEM climatology and spun up from rest for 20 years using climatological atmospheric forcing from ERA-40 (Uppala et al., 2005), with 3-hourly wind anomalies from the Fleet Numerical Meteorology and Oceanography Center 3-hourly Navy Operational Global Atmospheric Prediction System (NOGAPS) for the year 2003. The year

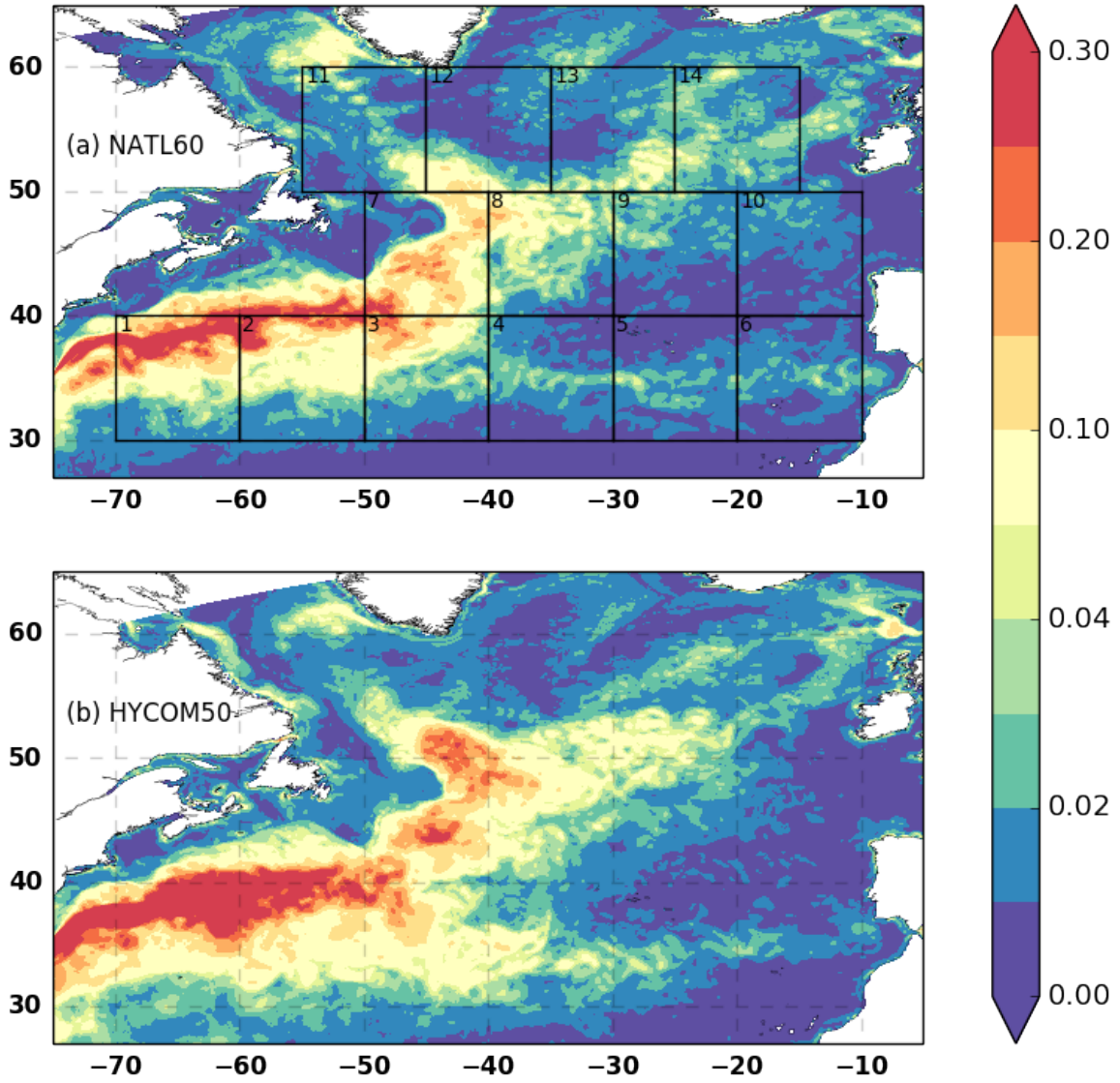

Figure 1: Surface eddy kinetic energy ($cm^2 s^{-2}$) computed from daily mean outputs of the total velocity. (a) NATL60 and (b) HYCOM50

2003 is considered to be a neutral year over the 1993 to present timeframe in terms of long-term atmospheric patterns the North Atlantic Oscillation. The last year of the simulation is used to perform the analysis. The horizontal viscosity operator is a combination of Laplacian and Biharmonic. The bathymetry is based on the Naval Research Laboratory (NRL) digital bathymetry database. The model configuration and a detailed evaluation of the model results in the Gulf Stream region with observations are documented in Chassignet and Xu (2017).

Table 1: Table of model parameters for NATL60 and HYCOM50

	NATL60	HYCOM50
Domain	26.5N - 65N	28 - 80N
Numerical Code	Nemo v.3.6	HYCOM
Horizontal grid	1/60: 0.9-1.6 km	1/50:1.1-2.2 km
Vertical coordinate	Z partial cells	Hybrid (Z & isopycnal)
Vertical grid	300 Levels : 1-50 m	32 Layers
Boundary conditions	GLORYS2v3	GDEM
Atmospheric forcing	DFS5.2	ERA-40
Horizontal Viscosity	Implicit in momentum advection	Laplacian & Biharmonic

Both NATL60 and HYCOM50 resolve the first Rossby radius of deformation everywhere within the model domains and these simulations reproduce realistic eddy statistics with levels of kinetic energy in the range of altimetric observations (Le Sommer et al., 2019; Chassignet and Xu, 2017) (Figure 1). HYCOM50 shows a higher eddy kinetic energy (EKE) level along and around the Gulf Stream-North Atlantic Current path. The less energetic Gulf Stream-North Atlantic Current in the NATL60 simulation may be due, in part, to its shorter spin-up period (6 months versus 19 years).

A summary of the model parameters is tabulated in Table 1. In this study, we consider the outputs of HYCOM50 for exactly the same region covered by NATL60 to have comparable results and we perform statistical analysis of the model outputs in two dimensional $10^\circ \times 10^\circ$ boxes, following earlier approaches by Stammer and Böning (1992), Uchida et al. (2017), and Chassignet and Xu (2017).

2.2 Wavenumber spectra

Wavenumber spectra provide a way to quantify the variability and energy associated with motions of different spatial scales across different regions. In this study, spectral analysis is performed in subdomains of $10^\circ \times 10^\circ$ boxes across the North Atlantic in order to document regional variability. Prior to spectral analysis, the field of each box is detrended in both direction and a 50% cosine taper window (turkey

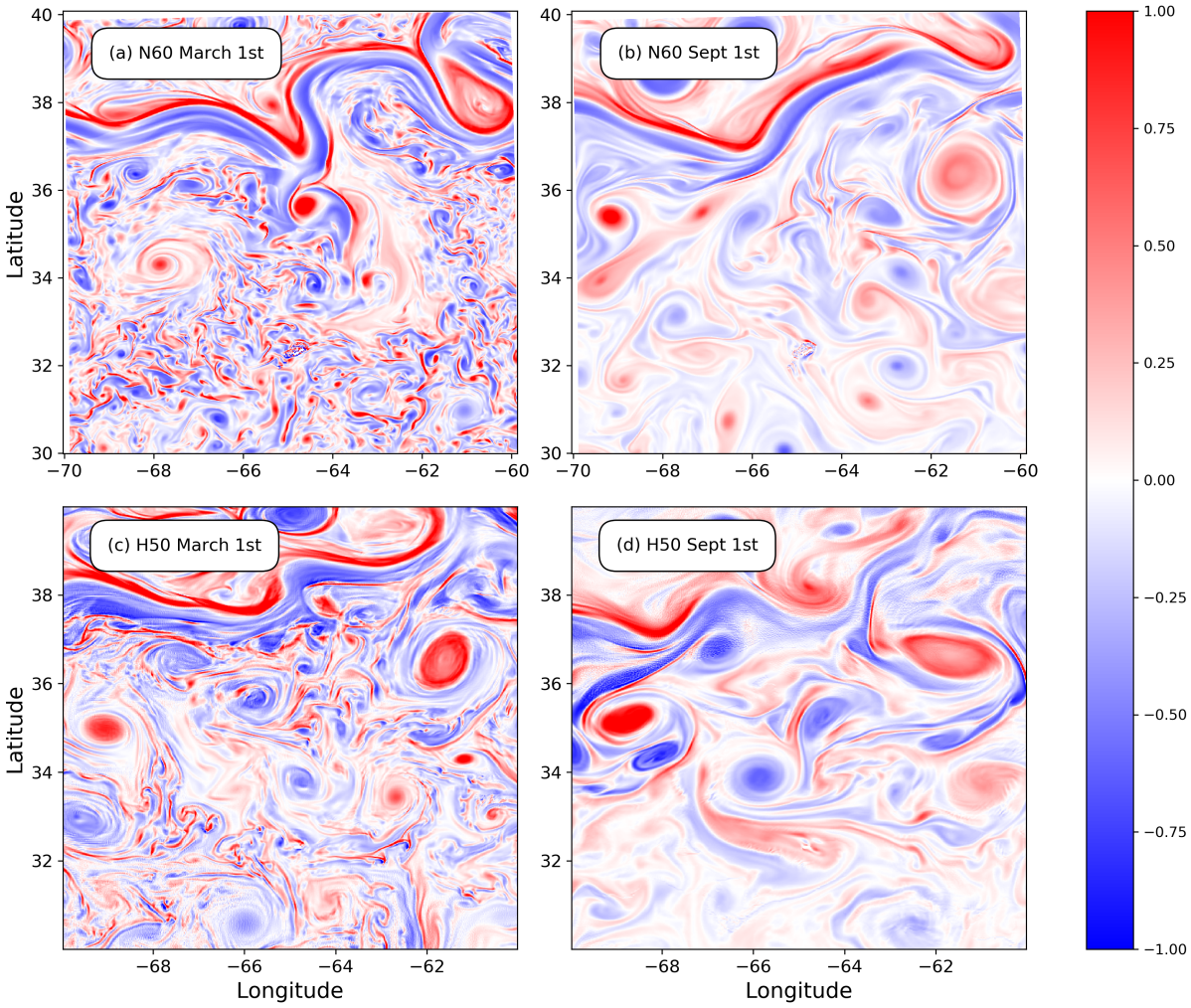

Figure 2: Seasonality of resolved vorticity field in NATL60 and HYCOM50 in Box 1

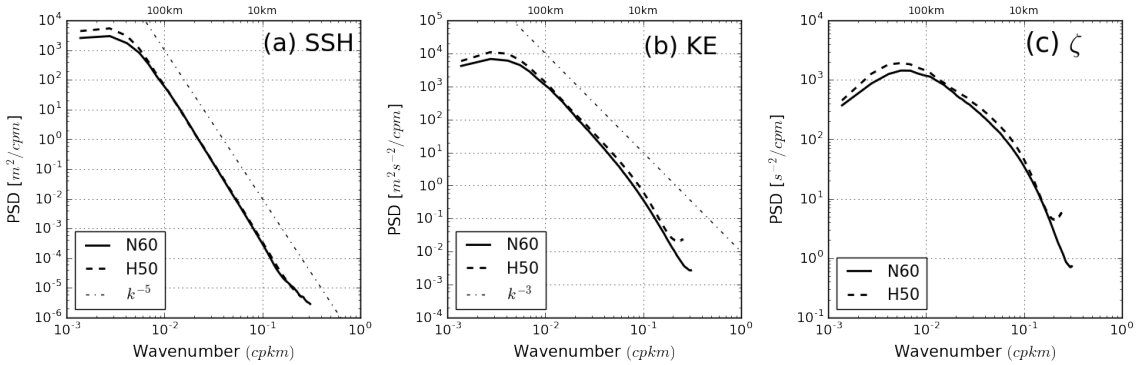

Figure 3: One year average wavenumber power spectra density in a 2D 10° square box (Box 1, Fig 1) around the energetic Gulf Stream region computed from daily output of NATL60 (thick black line) and HYCOM50 (thick dash line). (a) SSH (b) surface KE from total velocity (c) surface relative vorticity.

windowing) is applied for tapering. a Fast Fourrier Transform (FFT) is applied to the tapered data and a one-dimensional isotropic spectrum is obtained by averaging over all azimuthal directions. Our spectral approach is in line with Chassignet and Xu (2017) and because we are making use of year 20 of the HYCOM50 simulation used in Chassignet and Xu (2017), we were able to compare our SSH wavenumber spectra estimates with the already published results for the same dataset and found our result to be consistent as well (not shown).

Figure 3 shows the wavenumber power spectral density for SSH, surface kinetic energy (KE), and surface relative vorticity (RV) in a region close to the Gulf Stream (Box 1, as defined in Figure 1) for the two datasets. The wavenumber power spectra from the two models agree well, indicating that the distribution of energy across scales is similar in both models. The estimated slope from the SSH and KE spectra indicates that the two models agree with quasigeostrophic dynamics, which predict a slope of k^{-5} and k^{-3} for SSH and KE spectra, respectively. This agreement is particularly strong for the wavelength band of $10-100$ km. HYCOM50 shows more variance at low wavenumbers compare to NATL60. This is consistent with the lower EKE in NATL60 compared to HYCOM50 at these scales (Figure 1).

In Figure 4, we present the seasonality of SSH, KE, and RV wavenumber power spectral density. At scales smaller than 100 km, the variance of SSH, KE, and RV is of higher magnitude in winter (January, February, and March) compared to summer (July, August, and September). Whereas, the variance associated with scales larger than 100 km has a higher magnitude in the summer compared to winter. This winter-to-summer contrast is more pronounced in RV wavenumber spectra and is usually more visible in a winter-summer contrast of a RV snapshot (Figure 2).

The overall assessment shows that NATL60 and HYCOM50 agree reasonably well with each other on the dynamics governing the ocean surface. The small mismatch

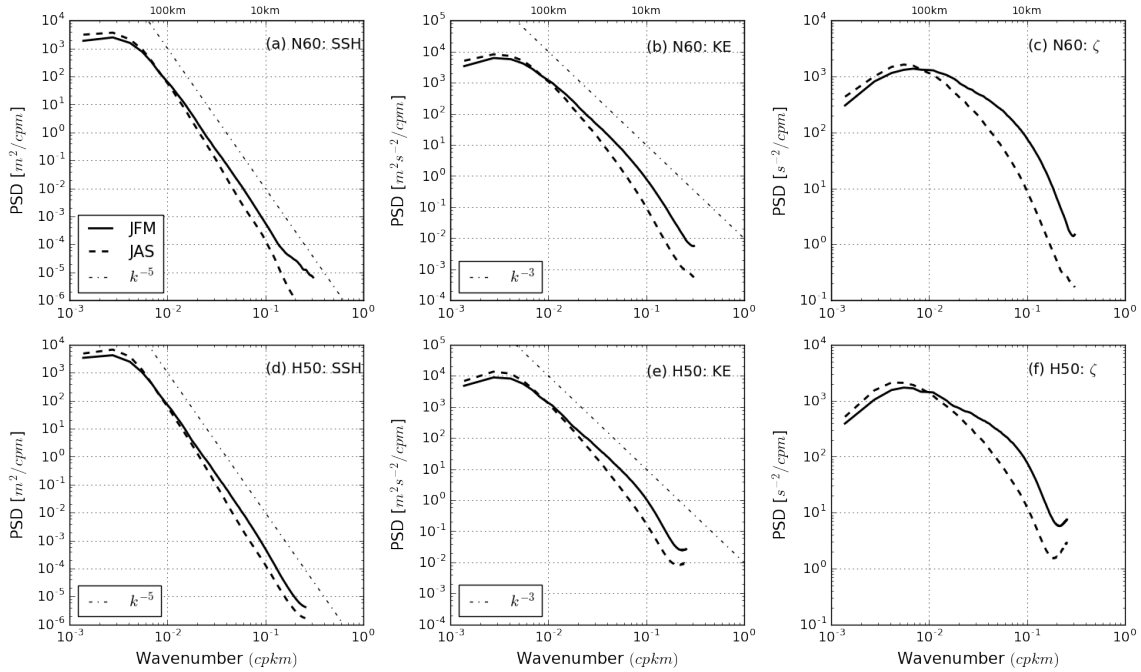

Figure 4: Winter (JFM) (thick black line) and summer (JAS) (thick dash line) wavenumber power spectra density in a 2D 10° square box (Box 1, Fig 1) around the energetic Gulf Stream region computed from daily output of NATL60 and HYCOM50.

between the result of the models may be a function of the differences in the model parameters and the length of their spin-up. In the next section, we focus on describing the statistics of eddy scales as seen in the two simulations.

2.3 Eddy length scale metric

A well-known approach for describing turbulent oceanic flows is to identify the typical length scale of motion that characterizes the dynamics of the flow. This involves computing the integral length scale of the energy-containing eddies (Qiu et al., 2014; Moum, 1996) or the enstrophy-containing scale (Scott, 2001; Morris and Foss, 2005) from the velocity and vorticity wavenumber spectrum, respectively. These length scales in physical space correspond to the scale of the most energetic eddy structures and are roughly consistent with the averaged scale of eddies that can be identified by eddy detection algorithms (Stammer, 1997; Chelton et al., 2007, 2011).

In this paper, we measure averaged eddy scales in each of our study regions by estimating the enstrophy-containing scale L_ζ from the vorticity wavenumber power spectra density following Scott (2001). The vorticity wavenumber spectral density is estimated (as described in section 2.2) using surface relative vorticity computed from the daily averaged model outputs. The enstrophy-containing scale is the enstrophy

weighted mean scale defined in equation (1) and it represents the scale of the most intense vortical structure in that flow. In equation (1), Z(k, l) denotes the vorticity wavenumber power spectral density, while k and l are the zonal and meridional wavenumber, respectively.

$$L_\zeta = \frac{\int\int Z(k,l)dkdl}{\int\int \sqrt{k^2+l^2}Z(k,l)dkdl} \tag{1}$$

To describe the distribution of the individual coherent eddy structures, we used an automated eddy detection algorithm. The algorithm detects coherent eddies by identifying closed SSH contours. A closed contour is then identified as an eddy if it satisfies some specific criteria with regards to its amplitude, number of pixels, the existence of at least one local extremum, etc. The successful application of the algorithm is documented in Chelton et al. (2011). This method is hereafter referred to as C11 and the corresponding eddy scale is referred to as L_η. We applied C11 to daily averages of SSH in two-dimensional 10° boxes for a period of one year. The implementation of the C11 algorithm in Python is available online at https://github.com/chrisb13/eddyTracking.

3 Description of eddy statistics

In this section, we present the variability of eddy statistics across the North Atlantic as diagnosed from the vorticity wavenumber spectra. The analysis is presented for both winter (January, February, and March) and summer (July, August, and September) in two regions: the Gulf Stream extension (Box 1) and the Labrador sea (Box 11). These two boxes were selected based on the fact that Box 1 is a well-documented high EKE region (Mensa et al., 2013) while Box 11 (a relatively low EKE region compare to Box 1) is a region with a very deep mixed layer in winter and energetic submesoscale activities.

In Figure 5, we show the vorticity wavenumber spectra for winter and summer in Box 1 and Box 11. In both boxes, vorticity wavenumber spectra vary notably from winter to summer, with the peak and enstrophy-containing scale (thick dot) of the spectra shifting to finer scales in winter. This change is evident in both models and in both regions. Similarly, the magnitude of the enstrophy-containing scale and spectra density vary from one region to another. The enstrophy-containing scale in Box 1 is of higher wavelength compared to Box 11. This type of regional difference in the spectra estimates and its weighted scale represents the spatial variability associated with the energy of the vortical structures across the North Atlantic. Regardless of the model or region, the winter spectra are shallower compared to the summer

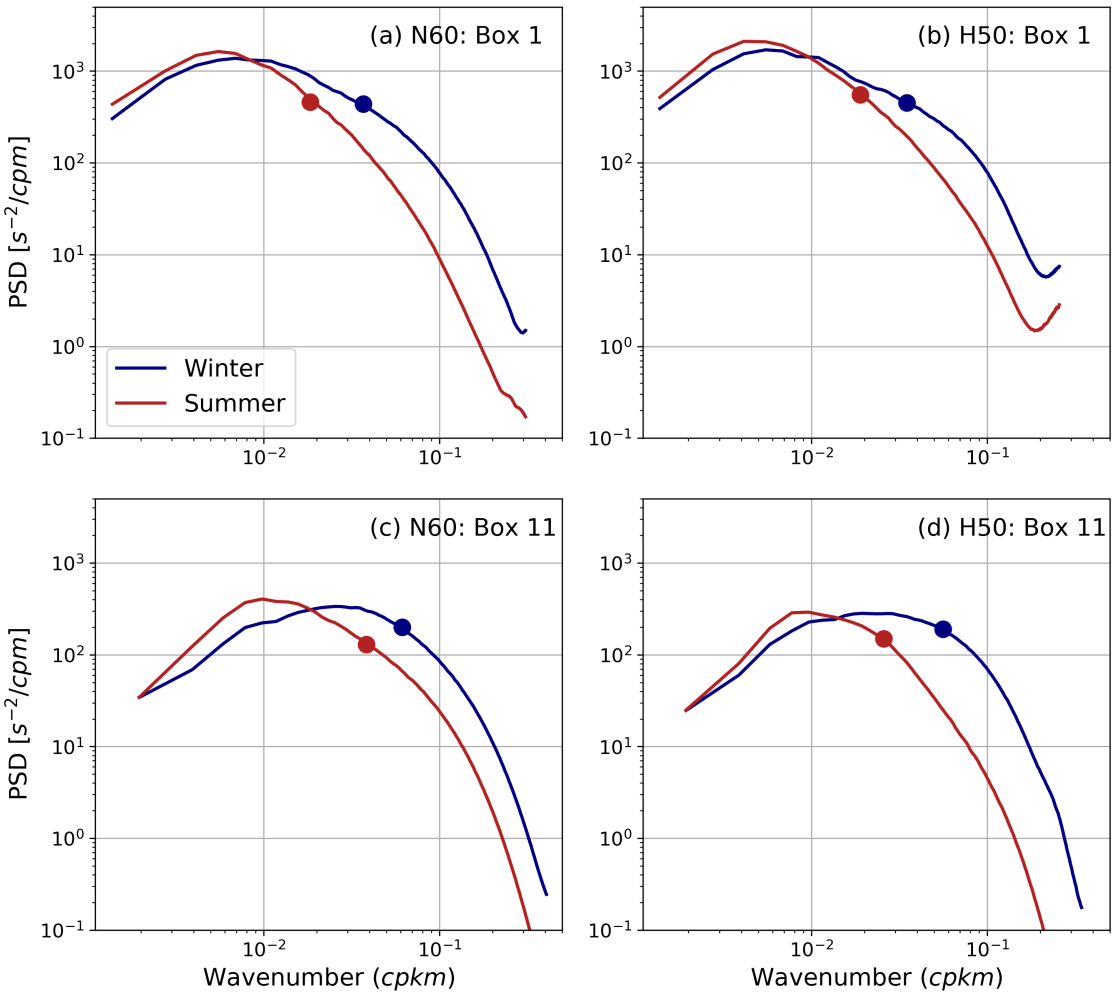

Figure 5: Surface relative vorticity wavenumber spectra for box 1 and box 11 (box defined in Figure 1), calculated from daily averages for winter time, JFM (red line) and summer time, JAS (blue line). Thick dot represent enstrophy-containing scale for each spectra. (a) NATL60 Box 1 (b) HYCOM50 Box 1 (c) NATL60 Box 11 (d) HYCOM50 Box 11.

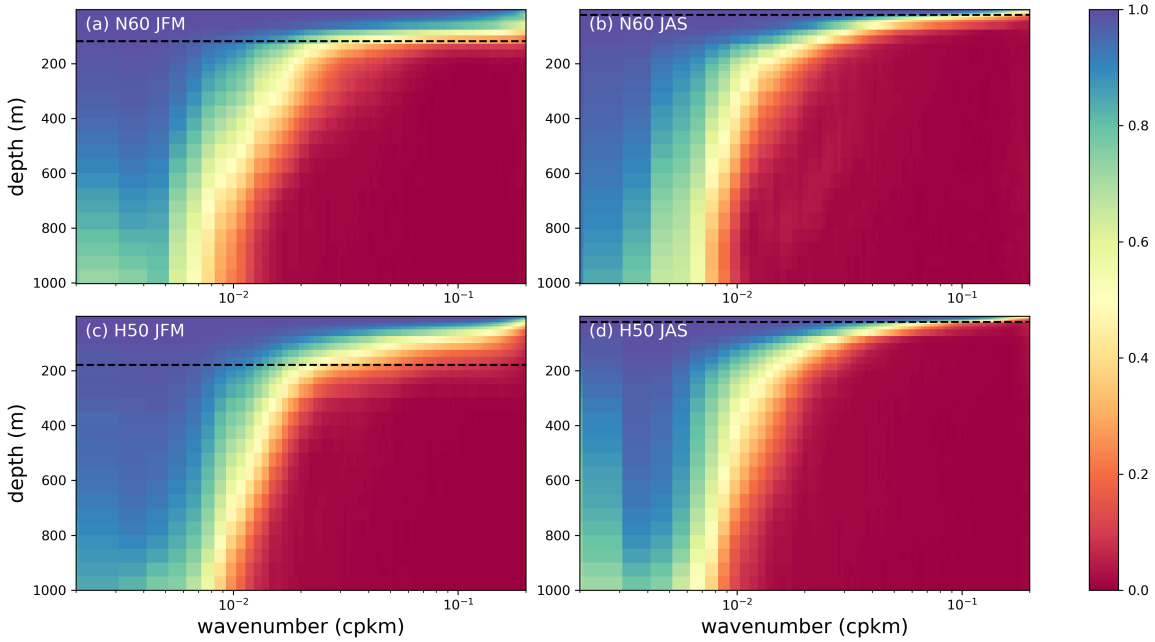

Figure 6: Winter and summer averages of vorticity spectral coherence as a function of depth for NATL60 and HYCOM50 in Box 1.

spectra (Figure 5), which indicates that energetic structures occupy a wider range of scales in winter. Also in winter, eddy motions with scales around 30 km can be as energetic as eddy motions with scales around 100 km.

In order to characterize the depth penetration of eddy structures, we estimate for typical length scale the phase relationship between the vorticity spectral density at the surface and in the interior down to 1000 m. This spectral correlation provides a proxy for the depth penetration of energetic surface structures (Klein et al., 2009). In Figure 6, we present the winter and summer averages of spectral correlation of vorticity in Box 1 for the two simulations. In both seasons and in the two models, we see that energetic motions with a scale larger than 100 km are strongly correlated down to a depth of about 1000 m. On the other hand, scales smaller than 100 km penetrate less into the water column with an observed seasonality. In fact, at these scales, surface motions are correlated with the interior roughly down to 170 m in winter and down to 40 m in summer. Scales of motions less than 50 km tend to penetrate slightly deeper into the water column in NATL60. These summer and winter depth penetration values coincide fairly with the average mixed layer depth in the two seasons. This indicates that mixed layer instability could be a possible modulator of the vertical structure of fine-scale eddy motions. Overall, despite the differences in vertical resolution (300 vertical z levels in NATL60 and 36 hybrid isopycnal layers in HYCOM50), it is worth noting that the two simulations agree fairly well in terms of depth penetration of eddies.

In order to explain the seasonality of the enstrophy-containing scale in terms of the statistics of isolated eddy structures, Figure 7 shows the distribution of eddy scales obtained from the application of C11 to SSH fields. The histogram show eddies with a lifetime greater than ten (10) days, in order to filter out short-lived features wrongly identified as eddies by the algorithm. In the plot, the seasonal differences in the distributions of the scales of eddies are more pronounced for eddies with scales smaller than 50 km. Following our definition of submesoscales eddies (SMEs) as eddies with scales from 10 km to 50 km, we find that the seasonality of enstrophy-containing scale is attributed to an increased population of SMEs in winter. This information is supported by our analysis for both models across the North Atlantic and is, therefore, a robust signal.

The increase in the number of detected SMEs in winter corroborates the large variance at a high wavenumber in the vorticity spectra (Figure 5). However, we should note that the information about SME seasonality from the application of C11 highlights only the coherent structures, while the results of the spectra at a high wavenumber might include the vorticity variance coming from fronts, filaments, and all other active submesoscales features other than coherent vortices.

Noticeable in Figure 7 is the discrepancy in the tails of eddy scale distribution. In particular, there are more large-scale eddies (> 50 km) in HYCOM50 compare to NATL60. This difference, observed in most of the boxes, may be due to the difference in the choices of the sub-grid closures used in the models and/or, as discussed later, evidence of a stronger inverse energy cascade in HYCOM50.

4 Spatial variability of eddy scale

The spatial variability of the eddy scale is documented by computing the annual mean of the enstrophy-containing scale (L_ζ) computed from daily relative vorticity spectra for each box. The values of the mean length scale in each of the boxes for the two models is presented in Figure 8. The averaged scale varies spatially with a factor of about 2 as you move from the south to north in the North Atlantic. This spatial variability is consistent in the two models, but HYCOM50 has an annual mean scale slightly larger than NATL60 in almost all the boxes. This is consistent with what is observed in Figure 7 where typical eddy scales are larger in HYCOM50 than in NATL60.

To better understand how the eddy scales compare with the Rossby radius of deformation, we present in Figure 9 a plot of the annual mean of L_ζ versus the estimate of the first Rossby radius of deformation. The deformation radius is estimated using the GLORYS2v3 datasets following the approach highlighted in Chelton et al.

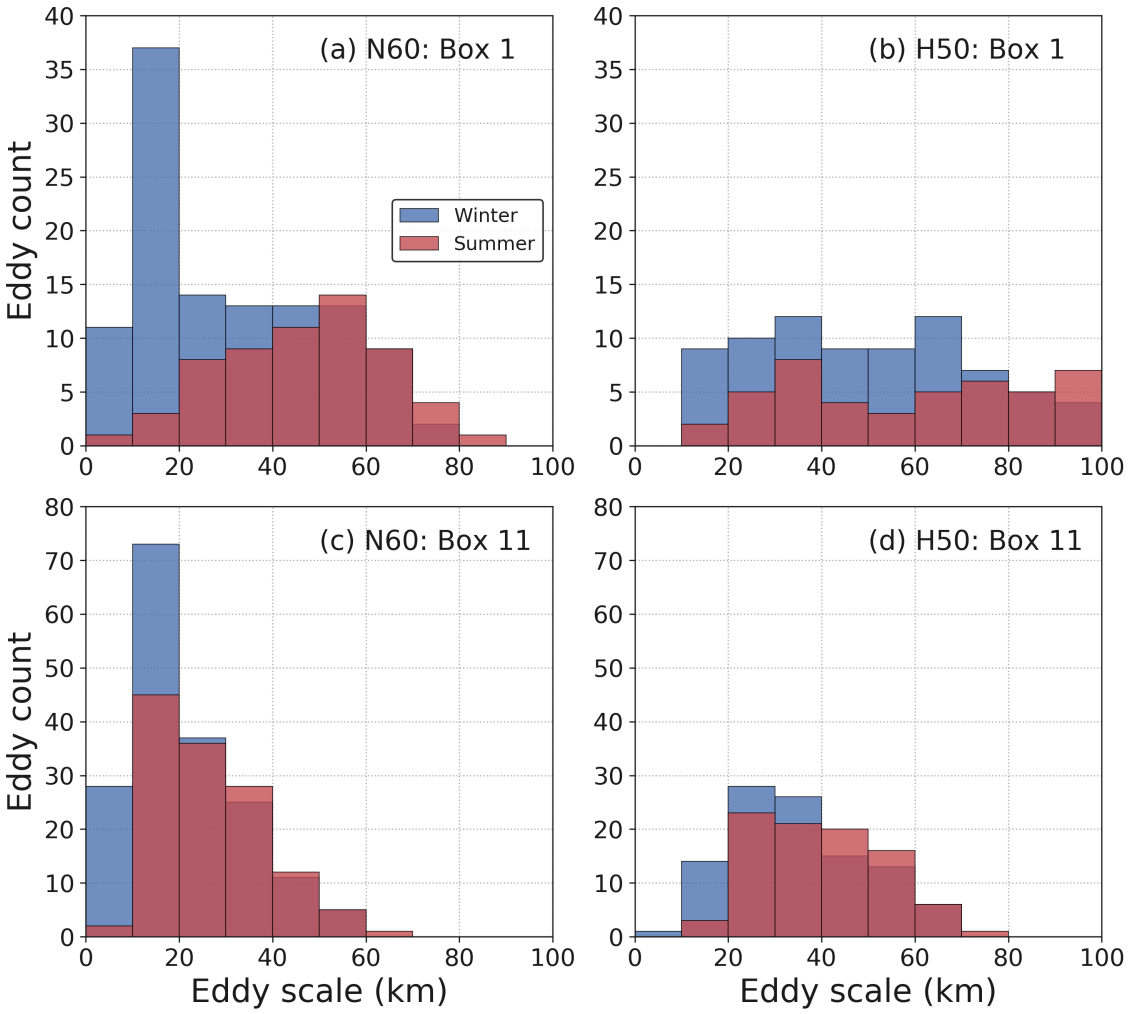

Figure 7: Histogram of eddy scale from eddy detection algorithm for box 1 and box 11 (defined in Figure 1), for winter time, JFM (red line) and summer time, JAS (blue line). (a) NATL60, Box 1 (b) HYCOM50, Box 1 (c) NATL60, Box 11 (d) HYCOM50, Box 11.

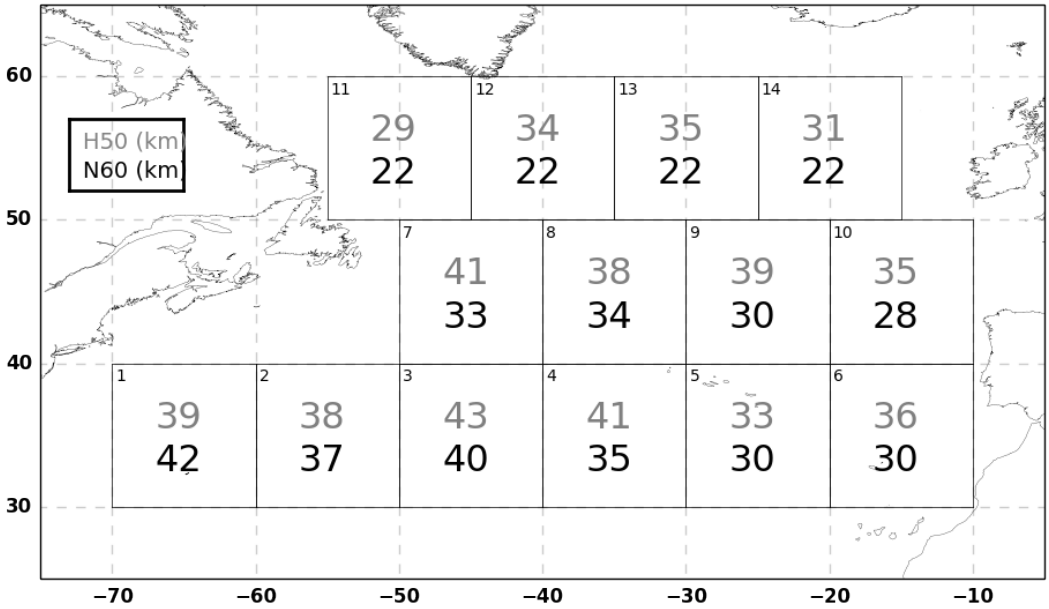

Figure 8: Map of one year averaged eddy scale (L_ζ) in all the 2D 10° boxes for NATL60 and HYCOM50

(1998). The spatial variability of the annually averaged scale is consistent with the estimate of the Rossby radius of deformation (L_d) with latitude (Figure 9). The length scales from HYCOM50 show less variability and this is evident in the slope of the fitted line plot (grey dash line). The slope for the annual averaged eddy scale is steeper for NATL60 (0.70) and shallower for HYCOM50 (0.27). The averaged eddy scale in winter is roughly consistent in the two models, while the difference in the annual mean of eddy scale between the two models is largely due to the difference in the scale of eddies in summer.

Following Klocker et al. (2016), we present a regime diagram for eddies identified from the application of C11 to SSH fields. The regime diagram presents a plot of eddy scale (L_η) normalised by the Rossby radius of deformation against a nonlinearity parameter ($r = U/c$) computed as the ratio of the root mean squared eddy velocity (U) and the Rossby wave phase speed ($c = \beta L_d^2$). The eddy velocity used in this study is the characteristic flow speed (U) within the eddy which is defined as the average geostrophic speed within the eddy interior (Chelton et al., 2007). $U = (g/f)(A/L)$, where g is the gravitational acceleration, f is the Coriolis parameter, A is the eddy amplitude and L is the effective radius of the eddy.

The regime diagram introduces frontiers along which the dynamical behavior of eddies is expected to change significantly (Klocker et al., 2016). Two different boundaries are considered in this study: (i) rotation dominated ($L/Ld < 1$) to stratification dominated ($L/Ld > 1$) and (ii) weak to strong Rossby elasticity which is represented by the Rhines scale (L_r). Figure 10 presents a kernel density plot

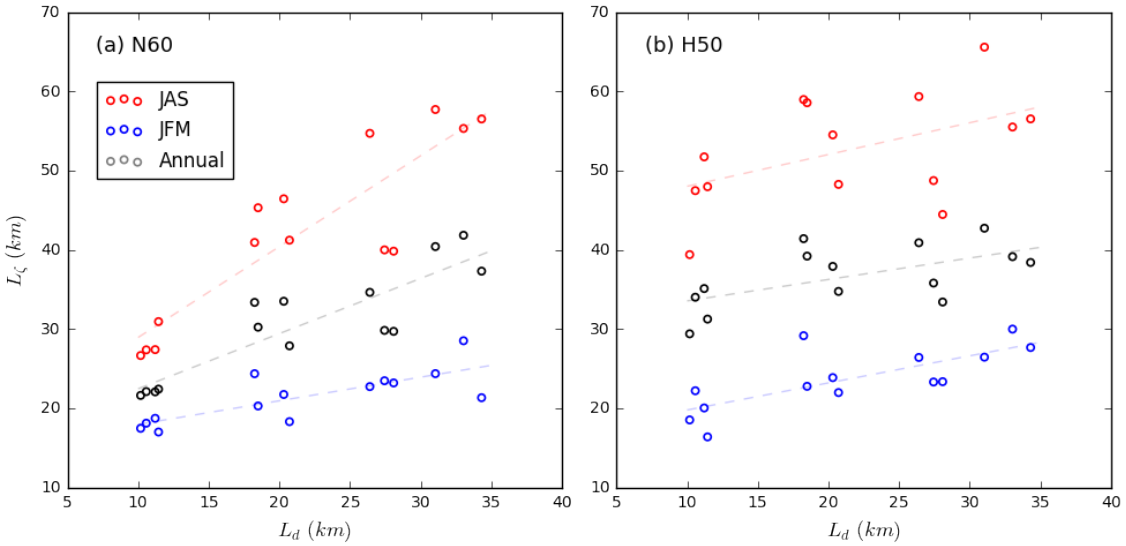

Figure 9: Eddy length scale L_ζ versus first baroclinic Rossby radius L_d. (a) NATL60 and (b) HYCOM50. Dash line represents estimated regression line and each circle corresponds to a averaged eddy scale in box.

and describes the relative position of eddies (as a function of eddy nonlinearity) to L_d and L_r. The first baroclinic Rossby radius of deformation defines the length scale of variability over which the internal vortex stretching is more important than relative vorticity (Chelton et al., 1998), while the Rhines scale can be thought of as a threshold of scale at which the inverse cascade of energy is arrested. The Rhines scale can also be interpreted as the scale where the dispersion of Rossby wave begins to dominate the ocean signal (Rhines, 1975).

Most of the detected eddies are nonlinear and the spread of eddy nonlinearity increases with latitude. The eddy scales lie between L_d and L_r which is consistent with the findings of Eden (2007), but the scales mostly follow the L_d for NATL60 (Figure 10a) while most scales in HYCOM50 are much bigger than L_d (Figure 10b). This difference follows from the argument presented in section 4 with regard to the abundance of eddies with larger scales in HYCOM50. Also, eddies in the 55^oN latitude band (grey shading) are more nonlinear in NATL60 compared to HYCOM50. One explanation could be that 55^oN latitude eddies in HYCOM50 are more elastic due to their bigger size (w.r.t to NATL60) and thus have smaller speed magnitude and hence smaller nonlinearity compared to NATL60. This could be interpreted as evidence of a stronger inverse cascade in HYCOM50, possibly because of the longer spin-up phase. The result from NATL60 is similar to that of Eden (2007) where the author argued that north of the 30°N, the eddy length scale should follow the Rossby radius of deformation and not the Rhines scale.

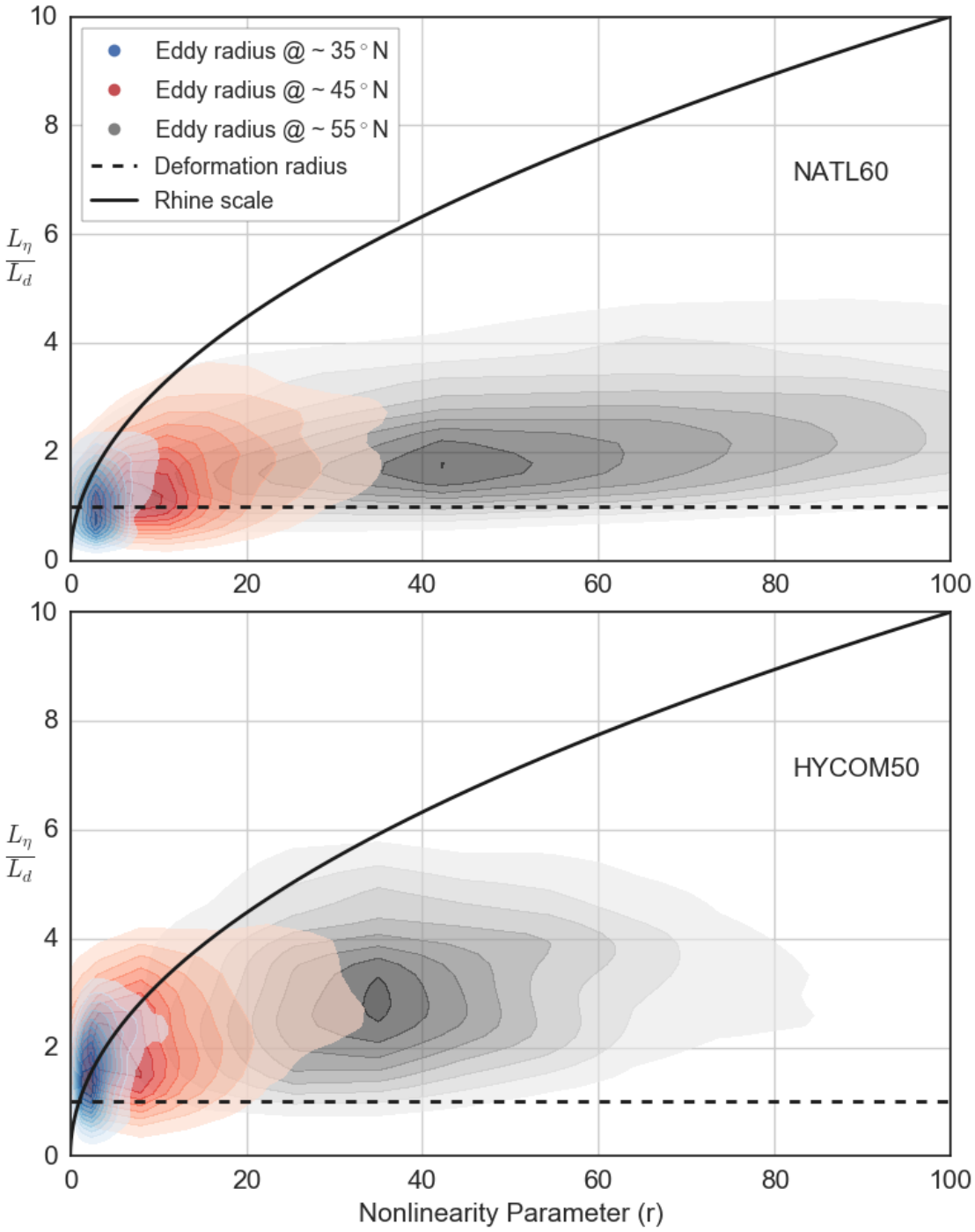

Figure 10: Kernel density plot of eddy nonlinearity (r) versus normalised eddy scale L_η/L_d for eddies identified by the automated eddy detection algorithm. The nonlinearity parameter (r) is defined as r = U/c following Chelton et al 2007. Colour blue, red and grey represents eddies in the 35°, 45°, and 55° latitudinal band. This regime diagram is adapted from Klocker et al. (2016). This plot combines data corresponding to 4680 and 3755 detected eddy structures for NATL60 and HYCOM50 respectively.

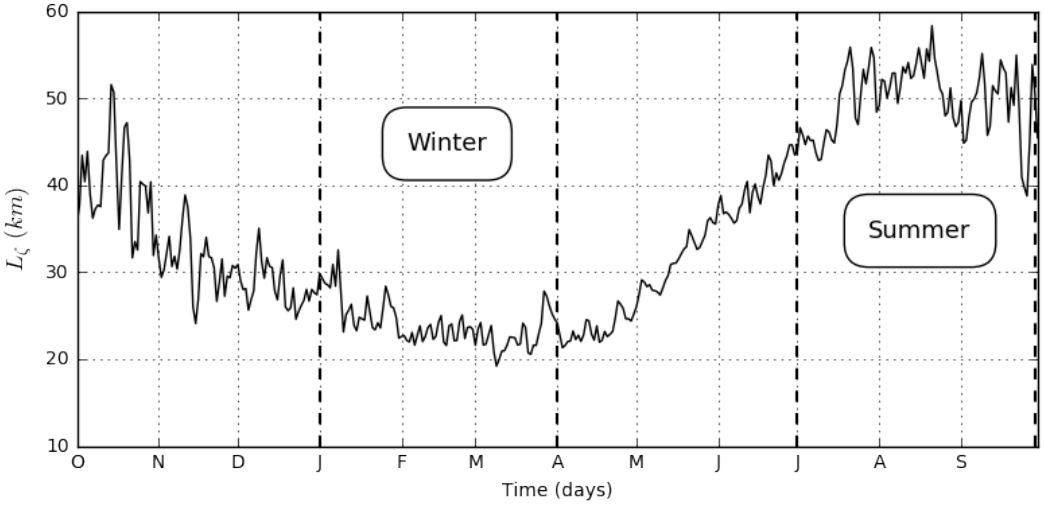

Figure 11: Time series of the enstrophy containing scale L_ζ for Box 1 (NATL60 dataset). The enstrophy containing scale is the enstrophy weighted mean scale defined in equation (1)

5 Temporal variability of eddy scale

In section 3 we established that scales of eddies undergo seasonal variability in the North Atlantic and that this seasonality is as a result of an increased population of submesoscale eddies ($10-50$ km) in winter. In Figure 11, we show the time series of L_ζ in Box 1, which illustrates the seasonality of eddy scale as captured by the enstrophy-containing scale defined in Equation (1). This seasonality is pronounced everywhere in the North Atlantic, as shown in Figure 12: The averaged eddy scale of L_ζ is about a factor of two larger in summer compared to winter. This reduction in scale from summer to winter is expected because there are more SMEs in winter that result in a smaller averaged eddy scales in winter.

So far we have shown that the average eddy scale varies in time across the entire North Atlantic following the seasonality of the number of SMEs. In what follows, we study the mechanism responsible for the seasonanlity of eddies from a dynamical point of view. Submesoscales are more active in wintertime (Thompson et al., 2016). Their emergence is believed to be driven by mechanisms such as frontogenesis, wind-induced frontal instabilities, and mixed layer instability among other processes (Thomas, 2008; McWilliams, 2016). Recent studies have identified baroclinic mixed layer instability (a specific frontal instability occurring in regions with a deep mixed layer and intense horizontal buoyancy gradients) as the dominant mechanism driving the emergence of submesoscale turbulence at mid-latitudes (Boccaletti et al., 2007; Fox-Kemper et al., 2008; Capet et al., 2008; Mensa et al., 2013; Sasaki et al., 2017)). Also, Uchida et al. (2017), using a mesoscale permitting ocean model on a global scale, surmised that mesoscale seasonality is a direct result of an inverse cascade

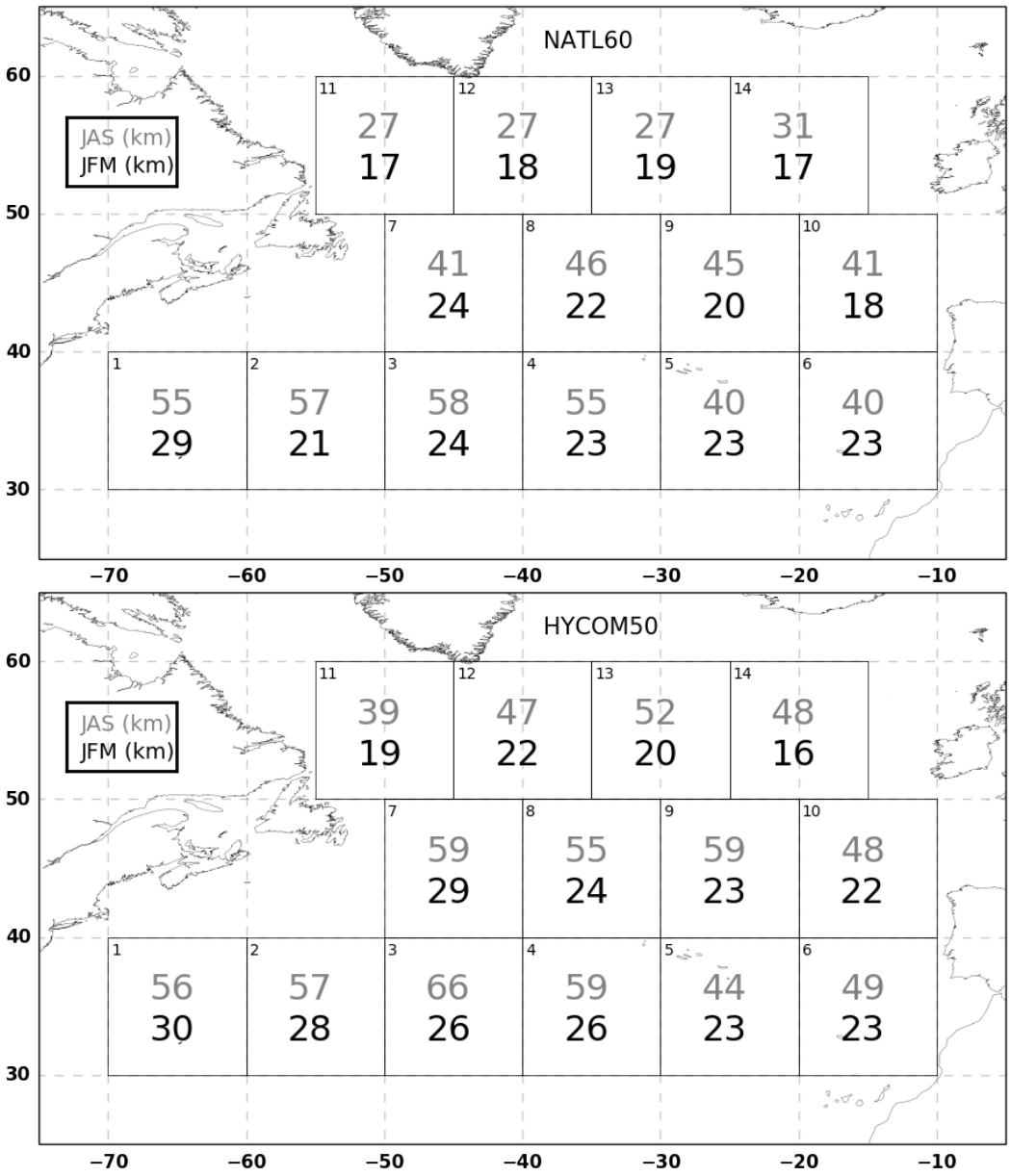

Figure 12: Map of averaged eddy length scale (L_ζ) in winter (JFM) and summer (JAS). (a) NATL60 and (b) HYCOM50

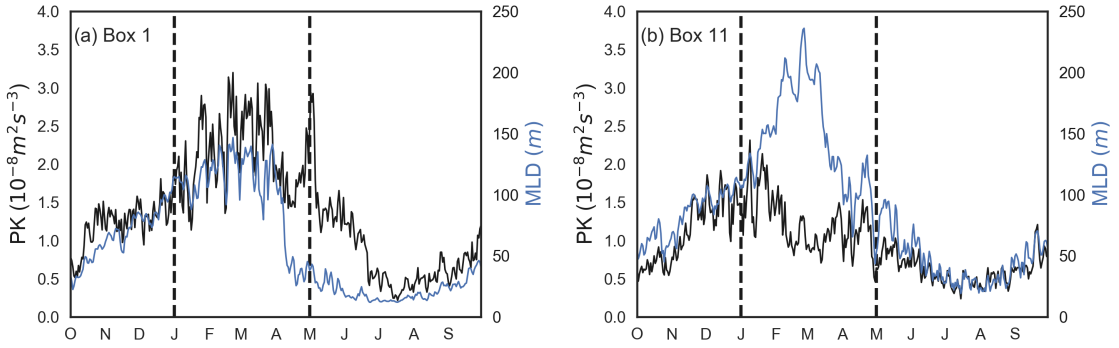

Figure 13: Time series of available potential energy, PK (blue line) and mixed layer depth, MLD (black line) for NATL60

of submesoscale energy generation by mixed layer instability. However, how the seasonality of submesoscales translates to the seasonality of SMEs is still unclear. This section aims to show that the increased population of SMEs in winter is directly linked to the advent of submesoscale turbulence in winter. Frontal structures that generate submesoscale eddies (Gula et al., 2016) exhibit high values of relative vorticity (Held et al., 1995). We intend to show the relationship between relative vorticity and submesoscale eddy statistics following a correlation of the later with mixed layer depth as shown in Sasaki et al. (2017).

In order to establish the relationship between the seasonality of submesoscale energy and eddy scale seasonality, we quantify the conversion of KE through baroclinic mixed layer instability following Boccaletti et al. (2007), Fox-Kemper et al. (2008), and Capet et al. (2008)). This conversion rate of available potential energy (APE) to eddy kinetic energy is defined as

$$PK \;=\; \frac{1}{h}\int_{0}^{-h} \langle w^{'} b^{'} \rangle_{xy} \; dz. \tag{2}$$

h, w, and b represent the mixed layer depth, vertical velocity, buoyancy gradient, respectively. The prime sign $[']$ indicates the small-scale component of the flow obtained by applying Lanczos windowing (with a cut frequency of 0.0125 and window size of 80 grid points) method to the two-dimensional fields of vertical velocity (w) and buoyancy (b).

Figure 13 presents the time series of mixed-layer depth (MLD) (blue line) and PK (black line) in box 1 and box 11 for NATL60. These two quantities are correlated with similar peaks in wintertime. This is consistent with previously published results of Boccaletti et al. (2007) and Sasaki et al. (2014) and this underscores mixed layer instability as the major driver for the emergence of submesoscale in winter.

We show similar time series for MLD (blue line), RV (red line) and daily counts

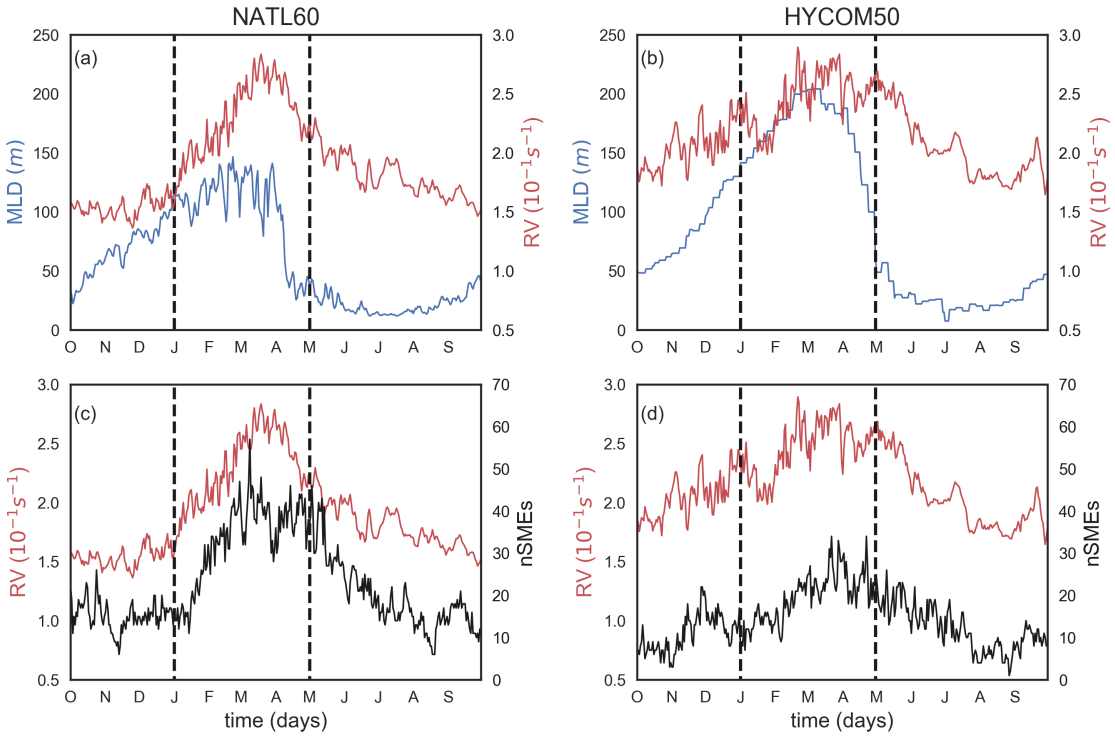

Figure 14: Time series of mixed layer depth, MLD (thin black line), root mean square of the surface relative vorticity RV (red line) and the number of submesoscale eddies (thick black line) in Box 1 for NATL60 and HYCOM50 datasets. nSMEs (daily number of L_η with a scale between 10km and 50 km)

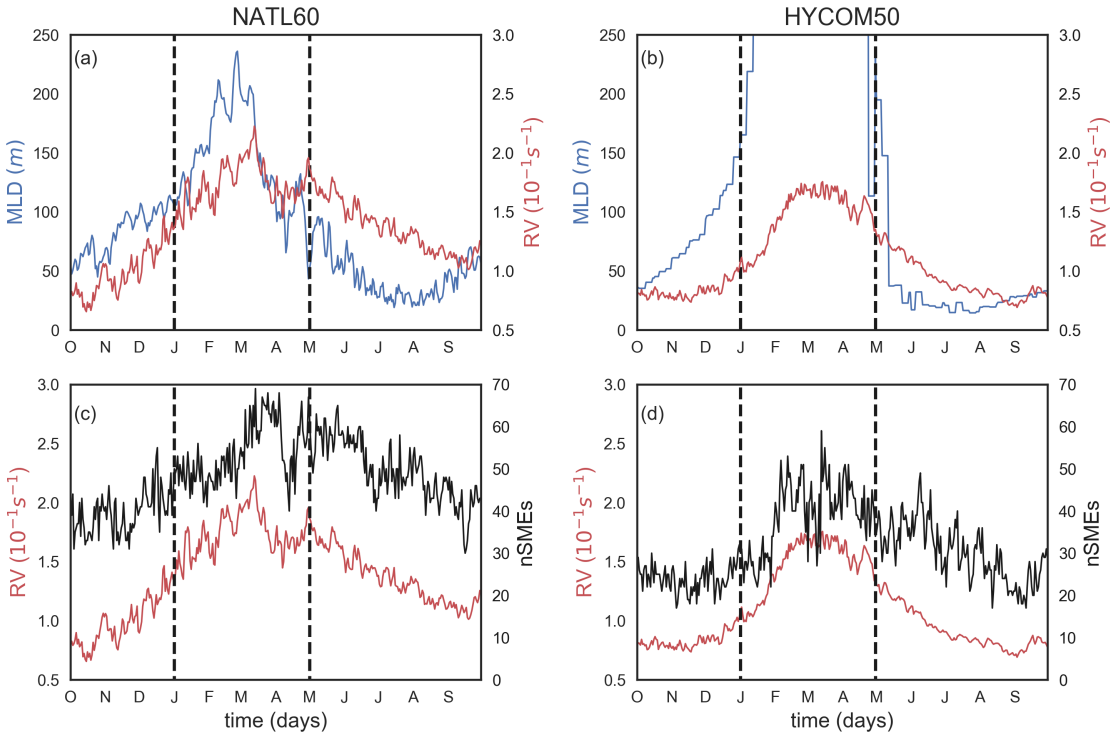

Figure 15: Time series of mixed layer depth, MLD (thin black line), root mean square of the surface relative vorticity RV (red line) and the number of submesoscale eddies (thick black line) in Box 11 for NATL60 and HYCOM50 datasets. nSMEs (daily number of L_η with a scale between 10km and 50 km)

of SMEs (thick black line) in Figure 14 and 15 for Box 1 and Box 11, respectively. Indeed, Figure 14a,b and 15a,b highlight how mixed layer instability drives the evolution of relative vorticity with a peak value in winter. An abrupt decay of MLD is observed in late winter that is not observed for RV. A similar result was recorded by Sasaki et al. (2017) and the authors attributed this difference in MLD and RV (starting in late winter) to the evolution of RV in two-dimensional turbulent flow in free decay after an abrupt decay of MLD. This implies that the dynamics immediately after wintertime is characterized by an inverse cascade of energy. This inverse cascade is evident in the subsequent decline in the number of submesoscale eddies in late winter (Figures 14c,d and 15c,d). It is, however, worth mentioning that SMEs and RV show a strong correlation with a similar peak in winter.

Figure 16 presents the vertical profile of eddy buoyancy fluxes $\langle w^{'} b^{'} \rangle$ in March and September for Box 1 and Box 11. We see seasonality in the profiles and this is associated with changes in mixed layer depth. The magnitude of $\langle w^{'} b^{'} \rangle$ in March is higher compared to September for the two simulations. A higher $\langle w^{'} b^{'} \rangle$ is responsible for feeding the growth and emergence of submesoscales eddies in winter. This growth is, however, region dependent. The winter-summer change in APE in Box 1 is about a factor of 3 higher than Box 11 for both NATL60 and HYCOM50.

6 Conclusion

The spatial and temporal variability of the typical size of oceanic eddies smaller than 100 km is investigated in this study using two submesoscale-permitting ocean model simulations of the North Atlantic NATL60 and HYCOM50. The scale of oceanic eddies shows a strong temporal and spatial variability as reflected in the enstrophy-containing scale estimated from the vorticity wavenumber spectra. Our analysis reveals that the increased population of submesoscale eddies (10 km - 50 km), driven by mixed layer instability in wintertime, is responsible for the seasonality of eddy scale in the North Atlantic. The winter/summer difference in the averaged eddy scale is about a factor of two in favor of summer. The map of averaged eddy scale reveals that the spatial variability of eddy length scale is consistent with the latitudinal dependence of the first Rossby radius of deformation and that most of the eddies 30°N of the North Atlantic are nonlinear in nature with a wider nonlinearity spread in the 55°N latitudinal bands. In terms of eddy penetration, we found that at scales less than 100 km the vertical structures of energetic eddy motion (diagnosed from the spectral coherence of vorticity) vary seasonally as a function of the mixed layer depth. In fact, the depth penetration of eddies with scales < 50 km is confined to the mixed layer. This further highlights how mixed layer instability modulates fine-scale dynamics.

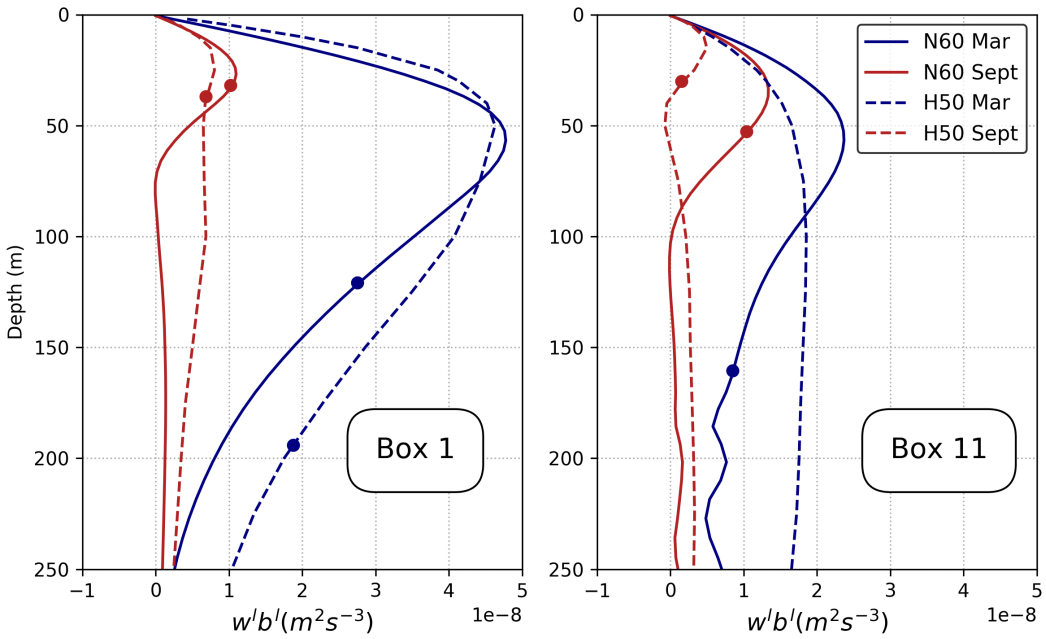

Figure 16: March (blue line) and September (red line) profile of $w'b'$ in Box 1 and Box 11 for NATL60 (thick line) and HYCOM50 (dashed line). Thick dot represent mixed layer depth.

While the focus of this study is to investigate eddy scale variability, we also examined the ability of NATL60 and HYCOM50 as a virtual observation scene for the SWOT mission. Following the analysis presented in this study and despite the model differences in terms of numerics, parameterization scheme, and vertical resolution, the statistics of eddy scale and the vertical structure of eddy motions captured by the two models are comparable. We can reasonably conclude that both NATL60 and HYCOM50 have the capability to resolve and characterize fine-scale dynamics down to 15 km scales in the North Atlantic, and that the fine-scale dynamics predicted by the models are a robust feature of this class of submesoscale permitting ocean models. This is key for the SWOT mission because information about eddy scale variability from these simulations (with respect to their horizontal resolution) is very useful for the calibration of inversion techniques for estimating two-dimensional maps of SSH from SWOT data. This knowledge of eddy scale variability will also be useful for improving eddy parameterization schemes of ocean models. However, there are concerns as to the size of the eddies identified in the models. The eddies are relatively smaller in NATL60 than in HYCOM50, and this is possibly a consequence of NATL60 short spin-up pahse (6 months) and smaller inverse energy cascade. In light of that, a longer run of NATL60 is recommended for future study to allow enough time for the simulated eddies to equilibrate.

References

Amores, A., Jorda, G., Arsouze, T., Le Sommer, J., 2018. Up to What Extent Can We Characterize Ocean Eddies Using Present-Day Gridded Altimetric Products? Journal of Geophysical Research: Oceans 123.

Bates, M., Tulloch, R., Marshall, J., Ferrari, R., 2014. Rationalizing the Spatial Distribution of Mesoscale Eddy Diffusivity in Terms of Mixing Length Theory. Journal of Physical Oceanography 44, 1523 – 1540.

Boccaletti, G., Ferrari, R., Fox-Kemper, B., 2007. Mixed Layer Instabilities and Restratification. Journal of Physical Oceanography 37, 2228 – 2250.

Brannigan, L., Marshall, D.P., Naveira-Garabato, A., George Nurser, A.J., 2015. The seasonal cycle of submesoscale flows. Ocean Modelling .

Bryan, F.O., 2008. Introduction: Ocean Modeling-Eddy or Not. Gophysical Mon. Series 177, 1 – 4.

Callies, J., Ferrari, R., Klymak, J.M., Gula, J., 2015a. Seasonality in submesoscale turbulence. Nature Communication 6, 6862.

Callies, J., Flierl, G., Ferrari, R., Fox-Kemper, B., 2015b. The role of mixed-layer instabilities in submesoscale turbulence. J. Fluid Mech. 788, 5 – 41.

Capet, X., Campos, E.J., Paiva, A.M., 2008. Submesoscale activity over the Argentinian shelf. Geophysical Research Letters 35, 2 – 6.

Chassignet, E.P., Xu, X., 2017. Impact of Horizontal Resolution (1/12 to 1/50) on Gulf Stream Separation, Penetration, and Variability. Journal of Physical Oceanography 47, 1999 – 2021.

Chelton, D.B., DeSzoeke, R., Schlax, M., El Naggar, K., Siwertz, N., 1998. Geographical Variability of the First Baroclinic Rossby Radius of Deformation. Journal of Physical Oceanography 28, 433 – 460.

Chelton, D.B., Schlax, M.G., Samelson, R.M., 2011. Global observations of nonlinear mesoscale eddies. Progress in Oceanography 91, 167 – 216.

Chelton, D.B., Schlax, M.G., Samelson, R.M., DeSzoeke, R., 2007. Global observations of large oceanic eddies. Geophysical Research Letters 34, 1 – 5.

Ducet, N., Traon, P.L., 2001. A comparison of surface eddy kinetic energy and Reynolds stresses in the Gulf Stream and the Kuroshio Current systems from merged TOPEX/Poseidon and ERS-1/2 altimetric data. J. Geophys. Res. 106, 16,603–16,622.

Ducousso, N., Le Sommer, J., Molines, J.M., Bell, M., 2017. Impact of the symmetric instability of the computational kind at mesoscale- and submesoscale-permitting resolutions. Ocean Modelling 120.

Dufau, C., Orsztynowicz, M., G., D., R., M., P.Y., L.T., 2016. Mesoscale resolution capability of altimetry: Present and future. J. Geophys. Res. Oceans 121, 1–18. doi:10.1175/JPO-D-11-0240.1.

Dussin, R., Barnier, B., Brodeau, L., Molines, J.M., 2018. The making of the DRAKKAR forcing set DFS5. Drakker .

Eden, C., 2007. Eddy length scales in the North Atlantic Ocean. Journal of Geophysical Research 112, C06004.

Fox-Kemper, B., Ferrari, R., Hallberg, R., 2008. Parameterization of mixed layer eddies. Part I: theory and diagnosis. . Journal of Physical Oceanography 6, 1145 – 1165.

Fresnay, S., Ponte, A.L., Le Gentil, S., Le Sommer, J., 2018. Reconstruction of the 3-D Dynamics From Surface Variables ina High-Resolution Simulation of North Atlantic. Journal of Geophysical Research: Oceans 123.

Fu, L.L., Chelton, D.B., Le Traon, P.Y., Morrow, R., 2010. Eddy Dynamics From Satellite Altimetry. Oceanography 23, 14–25.

Fu, L.L., Ubelmann, C., 2014. On the transition from profile altimeter to swath altimeter for observing global ocean surface topography. J. Atmos. Oceanic Technol 31, 560 568.

Gula, J., Molemaker, J., McWilliams, J.C., 2016. Submesoscale Dynamics of a Gulf Stream Frontal Eddy in the South Atlantic Bight. Journal of Physical Oceanography 46, 305 – 325.

Held, I.M., Pierrehumbert, R.T., Garner, S.T., Swanson, K.L., 1995. Surface quasi-geostrophic dynamics. Journal of Fluid Mechanics 282, 1 – 20.

Klein, P., Isem-Fontanet, J., Lapeyre, G., Roullet, G., Danioux, E., Chapron, B., Le Gentil, S., Sasaki, H., 2009. Diagnosis of vertical velocities in the upper ocean from high resolution sea surface height. Geophys. Res. Lett. 36, 1–5. doi:10.1029/2009GL038359.

Klocker, A., Abernathey, R., 2014. Global Patterns of Mesoscale Eddy Properties and Diffusivities. Journal of Physical Oceanography 44, 1030 – 1046.

Klocker, A., Marshall, D.P., Keating, S.R., Read, P.L., 2016. A regime diagram for ocean geostrophic turbulence. Journal of the Royal Meteorological Society .

Le Sommer, J., Molines, J.M., Albert, A., Brodeau, L., Ajayi, A.O., Gomez Navarro, L., Cosme, E., Penduff, T., Barnier, B., Verron, J., Brasseur, P., Rampal, P., Chassignet, E., 2019. NATL60: A North Atlantic ocean circulation model dataset based on NEMO for preparing SWOT altimeter mission, in prep. In preparation for Geoscientific Model Development. .

Le Traon, P.Y., Rouquet, M.C., Boissier, C., 1990. Spatial scales of mesoscale variability in the North Atlantic as deduced from Geosat data. Journal of Geophysical Research 95, 20267.

McWilliams, J.C., 2016. Submesoscale currents in the ocean. Proc. R. Soc. A 472, 20160117.

Mensa, J.A., Garraffo, Z., Griffa, A., Ozgokmen, T.M., Haza, A., Veneziani, M., 2013. Seasonality of the submesoscale dynamics in the Gulf Stream region. Ocean Dynamics 63, 923 – 941.

Morris, S.C., Foss, J.F., 2005. Vorticity spectra in high Reynolds number anisotropic turbulence. Physics of Fluids 17, 1 – 4.

Moum, J.N., 1996. Energy-containing scales of turbulence in the ocean thermocline. Journal of Geophysical Research: Oceans 101, 14095 – 14109.

Qiu, B., Chen, S., Klein, P., Sasaki, H., Sasai, Y., 2014. Seasonal Mesoscale and Submesoscale Eddy Variability along the North Pacific Subtropical Countercurrent. Journal of Physical Oceanography 44, 3079 – 3098.

Rhines, P.B., 1975. Waves and turbulence on a beta-plane. Journal of Fluid Mechanic 69, 417 443.

Rocha, C.B., Gille, S.T., Chereskin, T.K., M., D., 2016. Seasonality of submesoscale dynamics in the Kuroshio Extension. Geophysical Research Letters 43, 11304 – 11311.

Sasaki, H., Klein, P., Qiu, B., Sasai, Y., 2014. Impact of oceanic scale- interactions on the seasonal modulation of ocean dynamics by the atmosphere. Nature Communication 5, 5636.

Sasaki, H., Klein, P., Sasai, Y., Qiu, B., 2017. Regionality and seasonality of submesoscale and mesoscale turbulence in the North Pacific Ocean. Ocean Dynamics 67, 1195 – 1216.

Scott, R.B., 2001. Evolution of energy and enstrophy containing scales in decaying, two-dimensional turbulence with friction. Physics of Fluids 13, 2739 – 2742.

Stammer, D., 1997. Global characteristics of ocean variability estimated from regional TOPEX/ POSEIDON altimeter measurements. Journal of Physical Oceanography 27, 1743 – 1769.

Stammer, D., Böning, C.W., 1992. Mesoscale Variability in the Atlantic Ocean from Geosat Altimetry and WOCE High-Resolution Numerical Modeling.

Thomas, L., 2008. Submesoscale processes and dynamics. Geophysical Monograph Series 177. doi:https://doi.org/10.1029/177GM04.

Thompson, A., Lazar, A., Buckingham, C., Naveira Garabato, A., Damerell, G.M., Heywood, K.J., 2016. Open-Ocean Submesoscale Motions: A Full Seasonal Cycle of Mixed Layer Instabilities from Gliders. Journal of Physical Oceanography 46, 1285 – 1307.

Uchida, T., Abernathey, R., Smith, S., 2017. Seasonality of eddy kinetic energy in an eddy permitting global climate model. Ocean Modelling 118, 41 – 58.

Uppala, S.M., Kållberg, P.W., Simmons, A.J., Andrae, U., da Costa Bechtold, V., Fiorino, M., Gibson, J.K., Haseler, J., Hernandez, A., Kelly, G.A., Li, X., Onogi, K., Saarinen, S., Sokka, N., Allan, R.P., Andersson, E., Arpe, K., Balmaseda, M.A., Beljaars, A.C., van de Berg, L., Bidlot, J., Bormann, N., Caires, S., Chevallier, F., Dethof, A., Dragosavac, M., Fisher, M., Fuentes, M., Hagemann, S., Hólm, E., Hoskins, B.J., Isaksen, L., Janssen, P.A., Jenne, R., McNally, A.P., Mahfouf, J.F., Morcrette, J.J., Rayner, N.A., Saunders, R.W., Simon, P., Sterl, A., Trenberth, K.E., Untch, A., Vasiljevic, D., Viterbo, P., Woollen, J., 2005. The ERA-40 re-analysis. Q. J. R. Meteorol. Soc. 131, 2961–3012. doi:10.1256/qj.04.176.